

Ultrathin Layered Hydroxide Cobalt Acetate Nanoplates Face-to-Face Anchored to Graphene Nanosheets for High-Efficiency Lithium Storage

Liwei Su, Jinpei Hei, Xianbin Wu, Lianbang Wang,* and Zhen Zhou*

The dramatically increasing demand of high-energy lithium-ion batteries (LIBs) urgently requires advanced substitution for graphite-based anodes. Herein, inspired from the extra capacity of lithium storage in solid-electrolyte interface (SEI) films, layered hydroxide cobalt acetates (LHCA, $\text{Co}(\text{Ac})_{0.48}(\text{OH})_{1.52} \cdot 0.55\text{H}_2\text{O}$) are introduced as novel and high-efficiency anode materials. Furthermore, ultrathin LHCA nanoplates are face-to-face anchored on the surface of graphene nanosheets (GNS) through a facile solvothermal method to improve the electronic transport and avoid agglomeration during repeated cycles. Profiting from the parallel structure, LHCA//GNS nanosheets exhibit extraordinary long-term and high-rate performance. At the current densities of 1000 and 4000 mA g^{-1} , the reversible capacities maintain ≈ 1050 mAh g^{-1} after 200 cycles and ≈ 780 mAh g^{-1} after 300 cycles, respectively, much higher than the theoretical value of LHCA according to the conversion mechanism. Fourier transform infrared spectroscopy confirms the conversion from acetate to acetaldehyde after lithiation. A reasonable mechanism is proposed to elucidate the lithium storage behaviors referring to the electrocatalytic conversion of OH groups with Co nanocatalysts. This work can help further understand the contribution of SEI components (especially LiOH and LiAc) to lithium storage. It is envisaged that layered transition metal hydroxides can be used as advanced materials for energy storage devices.

1. Introduction

Lithium-ion batteries (LIBs) are currently the dominant choice for portable devices in terms of high energy/power density, good safety, and environmental compatibility.^[1–3] However, the low theoretical capacity (only 372 mAh g^{-1}) and unsatisfactory rate capability of commercial graphite anodes cannot meet the requirements of the dramatically increasing market. In the past decades, great efforts have focused on exploiting advanced substituted materials. Many inorganic materials have been developed according to four types of lithium storage mechanisms: Type I: insertion/extraction mechanism for TiO_2 and $\text{Li}_4\text{Ti}_5\text{O}_{12}$,^[4–6] Type II: alloying/dealloying mechanism for Si and Sn;^[7,8] Type III: conversion mechanism for transition metal oxides and sulfides;^[9–11] Type IV: electrocatalytic conversion mechanism for transition metal carbonates.^[12,13] However, the low capacity, poor ionic/electronic conductivity, and/or large volume swings of these materials seriously restrict their practical applications and, accordingly, various modifications

(focusing on doping, nanotechnology, and composites) can be adopted to overcome these shortcomings. Although extraordinary progress has been made, it is crucial and challenging to exploit better alternatives and, in particular, materials for novel lithium storage mechanisms.

For this purpose, we can gain enlightenment from the extra capacity phenomenon of transition metal oxides, which can deliver more lithium storage capacity (generally 10%–30%) than corresponding theoretical values.^[14] In 2002, Poizot et al. observed the significant extra capacity and clarified the reversible conversion of solid-electrolyte interface (SEI) films by transmission electron microscopy (TEM) and pseudocapacitive behaviors by electrochemical characterization. In recent investigations, we have further demonstrated that transition metal nanoparticles could serve as efficient electrocatalysts to activate and/or promote the reversible transformation of some inorganic components (especially Li_2CO_3) in SEI films, and hence contribute to increasing capacity for lithium storage.^[14] Grey and co-workers also showed that a major source of the extra capacity was the reversible reaction from LiOH (derived

Dr. L. Su, J. Hei, X. Wu, Prof. L. Wang
State Key Laboratory Breeding Base of Green
Chemistry-Synthesis Technology
College of Chemical Engineering
Zhejiang University of Technology
Hangzhou 310014, China
E-mail: wanglb99@zjut.edu.cn

Prof. Z. Zhou
Key Laboratory of Advanced Energy Materials Chemistry
(Ministry of Education)
Institute of New Energy Material Chemistry
Collaborative Innovation Center of Chemical Science
and Engineering (Tianjin)
School of Materials Science and Engineering
National Institute for Advanced Materials
Nankai University
Tianjin 300350, China
E-mail: zhouzhen@nankai.edu.cn



DOI: 10.1002/adfm.201605544

from $\text{RuO}_2 \cdot \gamma\text{H}_2\text{O}$ during discharge) to Li_2O and LiH under the existence of Ru metal nanoparticles, confirmed by high-resolution solid-state nuclear magnetic resonance (NMR) techniques together with theoretical computations.^[15] Furthermore, we notice that the chemical conversion of acetates can be efficiently conducted under electrocatalysis of transition metals or oxides.^[16–22] Therefore, it is envisaged that this conversion could also occur in LIBs. These observations enlighten us that, besides Li_2CO_3 , other SEI components, especially LiOH and lithium acetate (LiAc), should have a considerable potential for lithium storage if adopting effective metal catalysts. In particular, Co-based active materials (such as LiCoO_2 , LiCoPO_4 , CoO , and CoCO_3) are always preferred in LIBs. Thus, it is reasonable to design a compound consisting of Co^{2+} , Ac^- , and OH^- ions, which can convert into Co, LiOH , and LiAc during discharge processes, to confirm the proposal mentioned above. On the other hand, the designed compound should be a promising candidate for high-capacity lithium storage materials.

Layered hydroxide cobalt acetate (LHCA) belongs to the family of layered hydroxide metal acetates with the general formula $\text{M}(\text{Ac})_x(\text{OH})_{2-x} \cdot n\text{H}_2\text{O}$, where M is a transition metal, and x and n depend on the metals and preparation conditions.^[23–28] The unique layered crystal structure enables them to be outstanding anion-exchange and magnetic materials. LHCA possesses a layered structure with interlamellar distance of $\approx 10 \text{ \AA}$.^[23] The discharged components match the designed composition of materials mentioned above perfectly, i.e., $\text{Co} + \text{LiOH} + \text{LiAc}$, based on the conversion mechanism (Type III). Therefore, herein we introduce LHCA with the formula $\text{Co}(\text{Ac})_{0.48}(\text{OH})_{1.52} \cdot 0.55\text{H}_2\text{O}$ as a novel lithium storage material, to investigate the lithium storage potential of LiOH and LiAc . Fourier transform infrared (FT-IR) spectroscopy was performed to confirm the change of chemical compositions,

while electrochemical techniques were conducted to elucidate the reversibility in long-term and high-rate cycling. To improve the Li^+ /electron conductivity, LHCA was successfully prepared into ultrathin nanoplates and face-to-face anchored to graphene nanosheets (GNS) surface (denoted as LHCA//GNS hybrid nanosheets).

2. Results and Discussion

2.1. Materials Characterization of Pure LHCA

Herein, the LHCA compound was fabricated through a chimie douce (soft chemistry) method by dehydrating cobalt acetate tetrahydrate ($\text{Co}(\text{Ac})_2 \cdot 4\text{H}_2\text{O}$) in a solvothermal solution of ethylene glycol (EG). Chimie douce methods are performed under moderate conditions (typically $T < 500 \text{ }^\circ\text{C}$) during which the structural features of the reactants are preserved in the product, but the composition changes. This method is useful to modify the electronic structure of solids by doping and to design new metastable compounds by dehydration and ion exchange.

As shown in **Figure 1a**, the X-ray diffraction (XRD) pattern of pure LHCA shows a strong peak at a low degree of $\approx 10^\circ$ and various weak peaks at 13° – 60° , mismatching the standard cards of CoO , Co_3O_4 , CoCO_3 , $\text{Co}(\text{OH})_2$, $\text{Co}(\text{CO}_3)_{0.5}\text{OH}$, and $\text{Co}(\text{Ac})_2 \cdot 4\text{H}_2\text{O}$. The strong peak at around 10° manifests the lamellar characteristic of layered hydroxide metal acetates. According to Scherrer's equation, the interlamellar distance are calculated to be $\approx 10 \text{ \AA}$, which enables a high-efficiency cationic exchange for lithium storage. This characteristic peak can be clearly observed in the XRD patterns of LHCA/GNS composites and becomes weaker along with increasing the content of GNS samples (denoted as S1–S3). Thermogravimetric analysis (TGA,

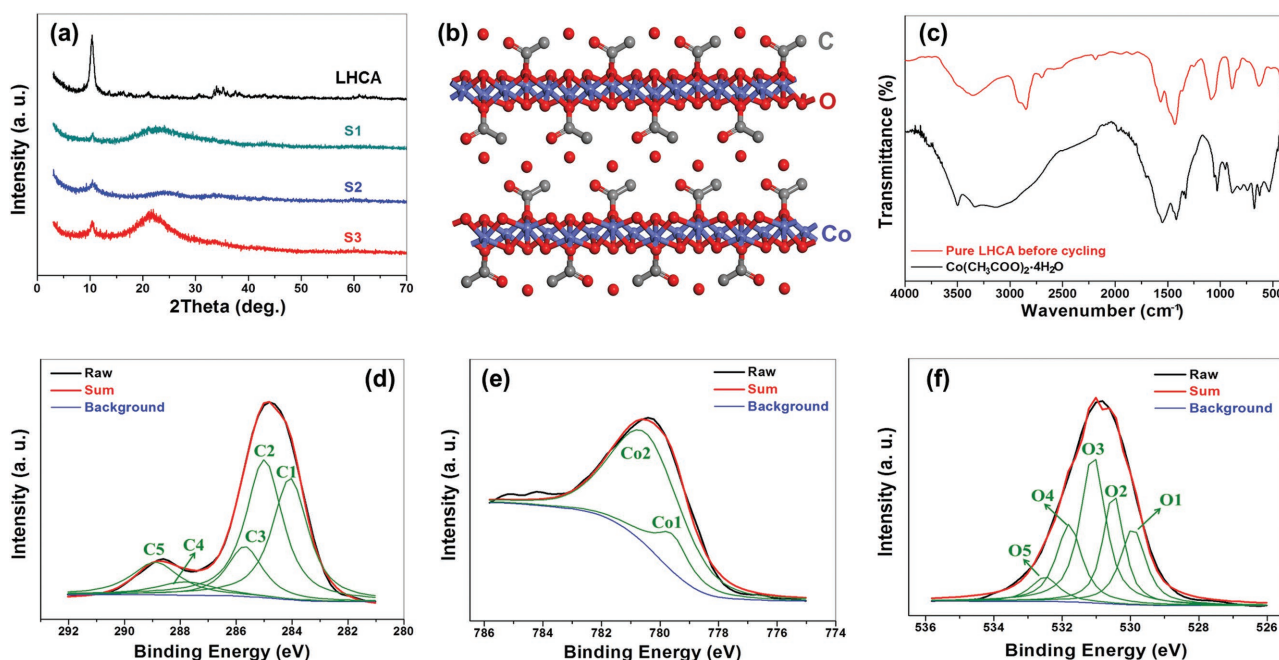


Figure 1. a) XRD patterns of pure LHCA and LHCA/GNS composites (S1–S3). b) Schematic diagram of crystalline framework of LHCA (without showing H atoms). c) FT-IR spectra of $\text{Co}(\text{Ac})_2 \cdot 4\text{H}_2\text{O}$ and pure LHCA before cycling. XPS of pure LHCA: d) C1s, e) $\text{Co}2p_{3/2}$, and f) O1s.

Figure S2, Supporting Information) shows that the weight contents of GNS in **S1** to **S3** are 32.0%, 21.3%, and 8.8%, respectively.

The layered features of LHCA are schematically illustrated in Figure 1b. Co^{2+} ions are aligned in rows in an octahedral environment of oxygen atoms of OH^- and/or Ac^- groups. Many water molecules are intercalated between the Co and O layers. Note that the schematic structure shown here refers to the structure in previous reports,^[23–27] but is not strictly accurate since $\text{M}(\text{Ac})_x(\text{OH})_{2-x} \cdot n\text{H}_2\text{O}$ is believed to be a microcrystalline material and lacks in a reliable structural characterization. Elementary analysis and energy dispersive spectroscopy confirm that LHCA is comprised of Co, C, O, and H, with a weight ratio of 47.91: 9.37: 39.41: 3.32, corresponding to $\text{CoC}_{0.96}\text{O}_{3.03}\text{H}_{4.08}$, i.e., $\text{Co}(\text{Ac})_{0.48}(\text{OH})_{1.52} \cdot 0.55\text{H}_2\text{O}$. This result is very close to $\text{Co}(\text{Ac})_{0.5}(\text{OH})_{1.5} \cdot 0.5\text{H}_2\text{O}$ reported by Zheng and co-workers,^[24] and $\text{Co}(\text{Ac})_{0.38}(\text{OH})_{1.62} \cdot 0.53\text{H}_2\text{O}$ reported by Jouini and co-workers.^[23] The slight difference in the number of Ac^-/OH^- groups and crystal water comes from the adopted preparation conditions, including solvents, temperatures, and durations.

The chemical components of LHCA can be further confirmed by FT-IR and X-ray photoelectron spectroscopy (XPS). Both are nondestructive techniques frequently used to evaluate the valence states of the material surface. Figure 1c shows the FT-IR spectra of pure LHCA and commercial $\text{Co}(\text{Ac})_2 \cdot 4\text{H}_2\text{O}$ (with >99 wt% purity). LHCA shares almost the same spectrum with $\text{Co}(\text{Ac})_{0.38}(\text{OH})_{1.62} \cdot 0.53\text{H}_2\text{O}$ reported by Jouini and co-workers.^[23] The peaks located at 1567 and 1365 cm^{-1} have a frequency separation $\Delta\nu = 202 \text{ cm}^{-1}$ and correspond to the antisymmetric (ν_{as}) and symmetric stretching (ν_{s}) vibrations of CO_2^- in acetate groups, respectively.^[23,24] The other peaks are assigned to $\text{Co}(\text{Ac})_{0.48}(\text{OH})_{1.52} \cdot 0.55\text{H}_2\text{O}$: 3348 cm^{-1} for $\nu_{\text{s}}(\text{O}-\text{H})$ of crystal water; 2940 cm^{-1} for $\nu_{\text{as}}(-\text{CH}_3)$, 2870 cm^{-1} for $\nu_{\text{s}}(-\text{CH}_3)$; 1085 cm^{-1} for $\nu_{\text{s}}(\text{C}-\text{C})$; and 1042 cm^{-1} for C–O stretching bands.^[29–31] We also compared the spectra of pure LHCA with $\text{Co}(\text{Ac})_2 \cdot 4\text{H}_2\text{O}$. The location of their main peaks is in good agreement with each other, whereas $\text{Co}(\text{Ac})_2 \cdot 4\text{H}_2\text{O}$ shows higher intensity in the range of 3500–2700 cm^{-1} (for O–H of crystal water and $-\text{CH}_3$) and 1700–1300 cm^{-1} (for C=O and C–O groups) due to the larger amounts of crystal water and acetates. XPS C1s spectra (Figure 1d) confirms the presence of various C-containing groups: C–C at 284.3 and 285.0 eV; C–OR at 285.6 eV; C=O at 287.8 eV; and C–O at 288.9 eV.^[32] The $\text{Co}2\text{p}_{3/2}$ signal at 779.6 and 780.5 eV indicates the existence of Co^{2+} ions (Figure 1e), while the O1s peaks manifest the states of oxygen: CoO/CoOOH at 529.9 eV; O^{2-} at 530.4 eV; $\text{Co}(\text{OH})_2$ at 531.2 eV; $-\text{OH}$ at 531.8 eV; and $-\text{C}=\text{O}/\text{C}-\text{O}$ at 532.5 eV (Figure 1f). All of the FT-IR and XPS results are consistent with the chemical composition of $\text{Co}(\text{Ac})_{0.48}(\text{OH})_{1.52} \cdot 0.55\text{H}_2\text{O}$. The TGA result in Figure S2 (Supporting Information) is consistent with this formula of LHCA.

2.2. Preparation and Structural Characterization of LHCA/GNS Composites

As shown in Figure S1a (Supporting Information), pure LHCA is comprised of irregular nanoplates connected with each other. The initial discharge and charge capacity of pure LHCA are 1695 and 796 mAh g^{-1} (Figure S1b, Supporting Information),

respectively, manifesting promising lithium storage potential. However, the reversible capacity rapidly decreases to $\approx 80 \text{ mAh g}^{-1}$ after 40 cycles, which is probably due to poor electronic conductivity and serious agglomeration. To overcome this obstacle, we introduced versatile GNS with excellent electronic transport and especially large surface area that is beneficial to adsorb cations/anions, form nanostructures, and prevent agglomeration and pulverization during preparation and repeated cycles.^[33–35] Different from the most common methods for GNS-based composites, the route adopted here was more facile without any modification of GNS ahead. $\text{Co}(\text{Ac})_2 \cdot 4\text{H}_2\text{O}$, GNS, and urea were well dispersed in the EG solution, and then underwent a short-time solvothermal treatment to form ultrathin LHCA nanoplates on the GNS surface. Urea has two significant functions herein: chelating with Co^{2+} ions, and simultaneously modifying the GNS surface by releasing NH_4^+ ions. Similarly, EG possesses strong ability to capture Co^{2+} ions.^[36]

GNS here has two main functions in the composites: improving the electronic conductivity of LHCA and serving as a high-surface-area support to load LHCA for better distribution. As shown in Figure 2, the morphology and distribution of LHCA seriously depends on the content of $\text{Co}(\text{Ac})_2 \cdot 4\text{H}_2\text{O}$, from 0.063 g (**S1**), to 0.147 g (**S2**), and 0.566 g (**S3**). For **S1**, uniform LHCA nanoplates (<20 nm in thickness) are tightly attached to the GNS surface in parallel and denoted as LHCA//GNS nanosheets (Figure 2a,d). The face-to-face contact between LHCA nanoplates and GNS nanosheets benefits the electronic transport and avoids the agglomeration during repeated discharge/charge processes. Although **S2** consists of uniform LHCA nanoplates with similar thickness and larger area (Figure 2b,e), only the nanoplate edge anchors on GNS and cannot provide ideal electronic network like the face-to-face model in **S1**. When further increasing the content of $\text{Co}(\text{Ac})_2 \cdot 4\text{H}_2\text{O}$ to 0.566 g (**S3**), tremendous LHCA nanoplates seriously agglomerate into micrometer-scale materials on the GNS surface so that it is difficult to observe the presence of GNS (Figure 2c,f). The enhanced electronic conductivity from GNS was confirmed by electrochemical impedance spectroscopy (EIS, Figure S3, Supporting Information). The LHCA/GNS composites are preferable for enhancing the Li^+ /electron transport and avoiding the possible volume variation during cycling.

Atomic force microscope (AFM) shows that the average thickness of GNS is $\approx 0.660 \text{ nm}$, corresponding to three-layered GNS (Figure 3a). TEM images further reveal that three to four-layered nanostructures dominate the GNS sample (Figure 3b,c). As shown in Figure 3d,e, LHCA nanoplates are homogeneously pasted on the broad graphene surface without any agglomerates. The surface area of LHCA nanoplates is generally $0.1 \mu\text{m} \times 0.2 \mu\text{m}$, or larger. No obvious crystalline lattice can be found in the high-resolution TEM (HRTEM) image of LHCA nanoplates (Figure 3f). Also, no diffraction dots or rings are observed in the image of selected area electron diffraction (SAED), indicating the microcrystalline characteristic of anchored LHCA nanoplates.

2.3. Electrochemical Lithium Storage Performances of LHCA/GNS Composites

The samples were prepared into working electrodes and tested within the range of 3.0–0.01 V (vs Li/Li^+). As shown

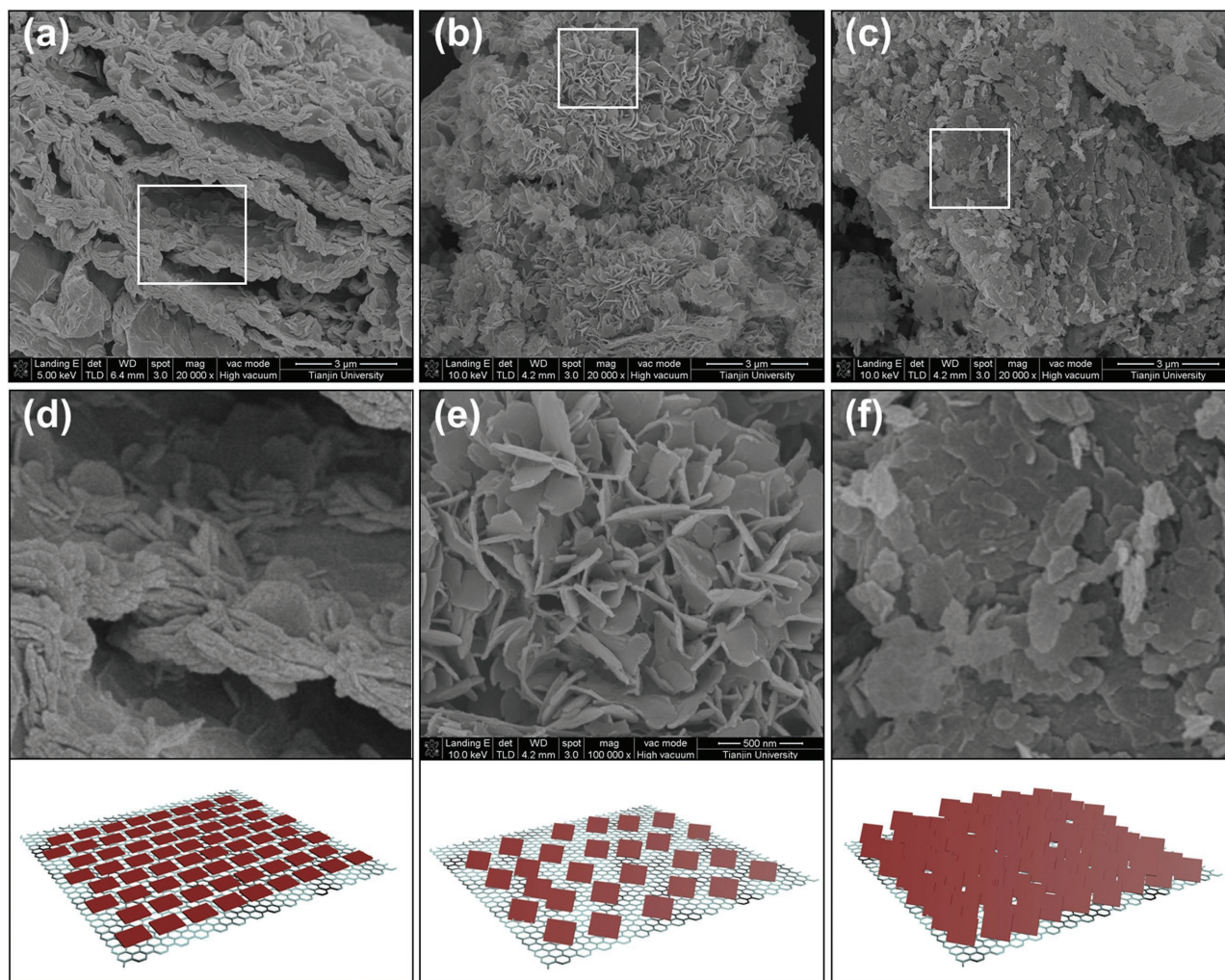


Figure 2. Scanning electron microscope (SEM) images of LHCA/GNS nanocomposites: a) **S1**, b) **S2**, and c) **S3**. d–f) Amplified SEM images and diagrams, corresponding to the white frame regions in (a)–(c), respectively.

in **Figure 4a**, the initial discharge and charge capacity of LHCA//GNS nanosheets (**S1**) are 2526 and 1216 mAh g⁻¹, respectively, at a current density of 200 mA g⁻¹. It is clear that the initial discharge curve is different from those of other cycles. The large slope above 0.7 V is mainly assigned to the formation of SEI films, which subsequently serve as positive layers to enhance Li⁺ transport and protect active particles from erosion outside. In the following cycles, the voltage slope (>0.7 V) greatly weakens, indicating that SEI films generally grow in the initial discharge. The reversible capacity gradually decreases to 1035 mAh g⁻¹ after 40 cycles with a loss of only 0.37% per cycle. Note that the tested capacity was calculated on the basis of the whole composites rather than pure LHCA (68.0 wt%). The reversible capacity of GNS is lower than 600 mAh g⁻¹ after 40 cycles (**Figure S4**, Supporting Information). If the contribution (<600 × 32.0% = 192 mAh g⁻¹) of GNS is excluded, the LHCA component in LHCA//GNS composites actually presents a much higher reversible capacity of ≈1240 mAh g⁻¹ after 40 cycles. When the LHCA content increases to 78.7 wt% (**S2**) and 91.2 wt% (**S3**), the reversible capacities are 910 and

704 mAh g⁻¹, respectively. The regressed capacity comes from the lower electronic conductivity and the exasperated agglomeration as the LHCA content increases. As shown in **Figure 2**, the microstructures of **S1–S3** are obviously different from each other. The face-to-face contact between LHCA nanosheets and GNS nanosheets in **S1** benefits the electronic transport and avoids the agglomeration during repeated discharge/charge processes. By contrast, only the edge of LHCA nanosheets anchors on GNS of **S2** and cannot provide ideal electronic network like **S1**. For **S3**, **Figure 2c,f** shows that the content of LHCA is too much to observe the presence of GNS.

A noteworthy doubt is the dissolution of LHCA, i.e., it might gradually dissolve in the electrolyte and cause serious structural damage especially in long-term and high-rate cycling tests. To address this crucial point, LHCA//GNS nanosheets (**S1**) were tested at high rates and cycled for 120 cycles (**Figure 4b**). At 350 mA g⁻¹ (≈1 C for the high-quality commercial graphite anode), the initial reversible capacity is 1060.8 mAh g⁻¹ and decreases to ≈740 mAh g⁻¹ after 40 cycles. Interestingly, the capacity gradually recovers to ≈970 mAh g⁻¹ in the subsequent

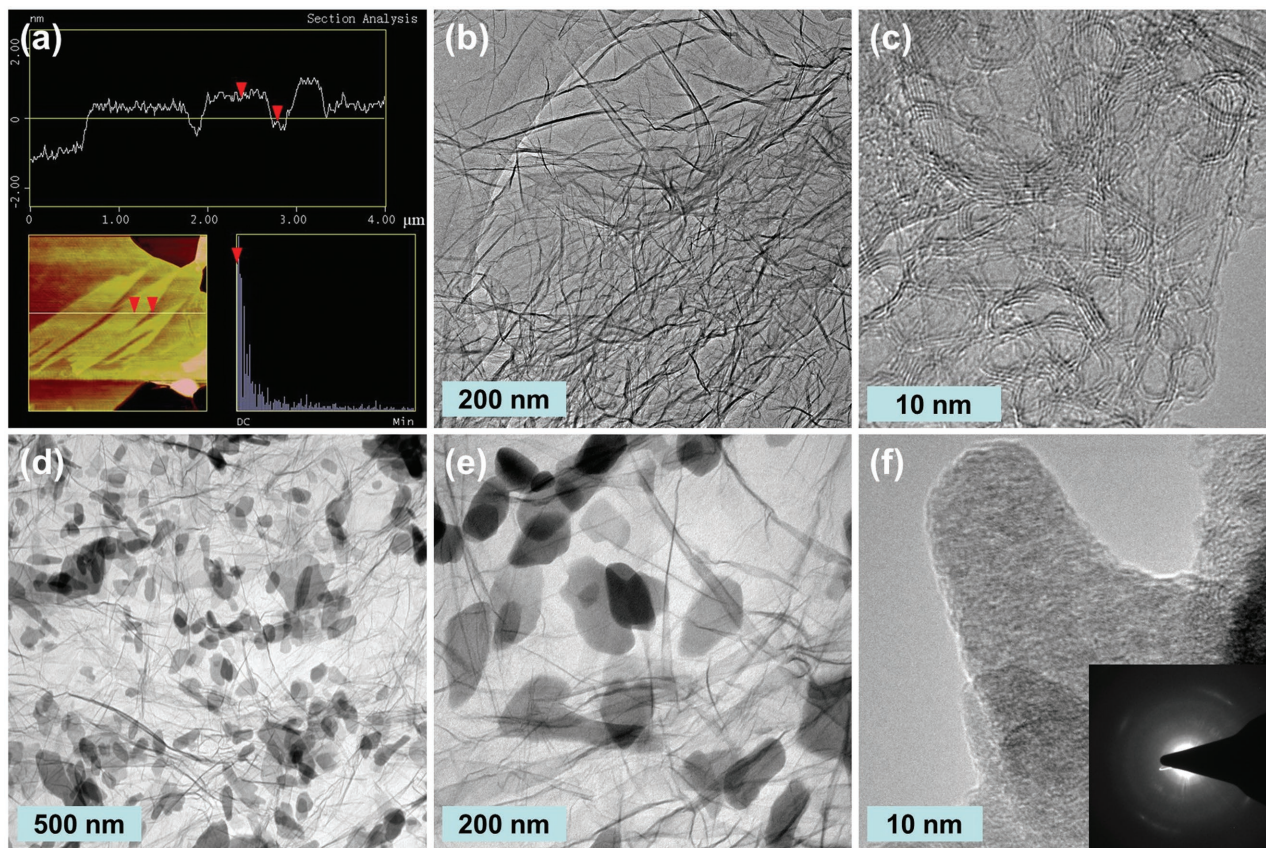


Figure 3. a) AFM and b,c) TEM images of few-layered GNS. d,e) TEM and f) HRTEM and SAED of LHCA//GNS hybrid nanosheets (S1).

80 cycles due to the enhanced activation and reversible transformation of some SEI components.^[37] The Coulombic efficiency maintains $\approx 98\%$ after the initial 10 cycles. Figure 4c shows the high-rate performance of S1 at 1000 and 4000 mA g^{-1} .

At 1000 mA g^{-1} , the reversible capacity keeps $\approx 600 \text{ mAh g}^{-1}$ for the first 100 cycles and increases to $\approx 1050 \text{ mAh g}^{-1}$ in the following 100 cycles. Similarly, at a higher current density of 4000 mA g^{-1} , the reversible capacity is 300–350 mAh g^{-1} for

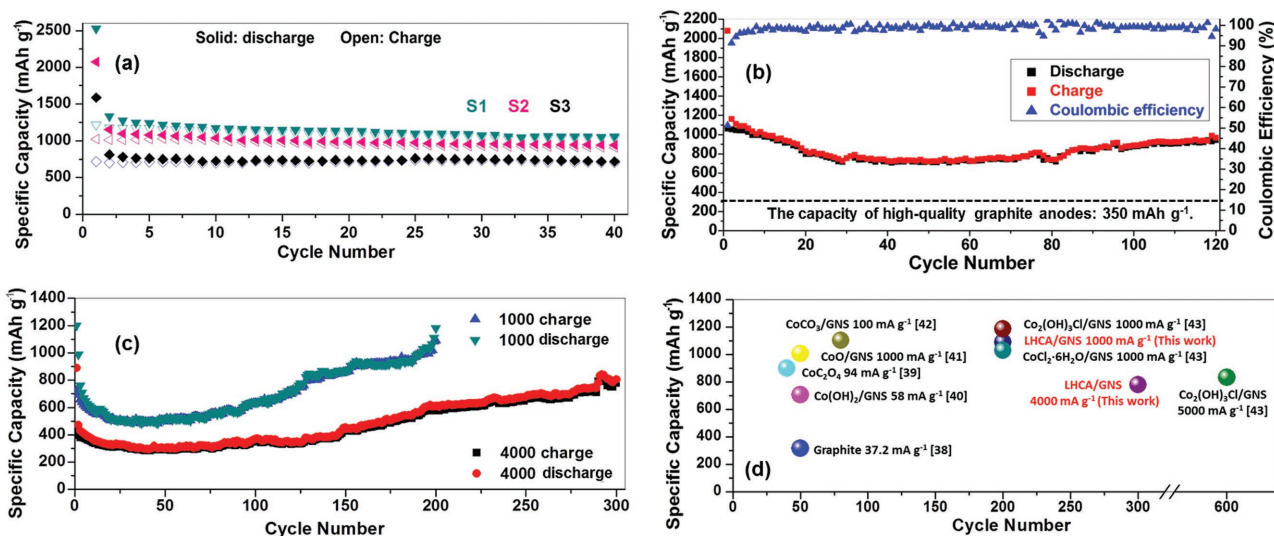


Figure 4. a) Cycling performances of S1–S3 at the current density of 200 mA g^{-1} . b) Long-term cycling performances and Coulombic efficiency of S1 at 350 mA g^{-1} (dotted line: the capacity of high-quality commercial graphite, $\approx 350 \text{ mAh g}^{-1}$). c) High-rate performance of S1 at 1000 and 4000 mA g^{-1} . d) Comparison of electrochemical performances among LHCA//GNS (S1), high-quality graphite, and the most representative Co(II)-based materials.

the initial 140 cycles and gradually levels up to $\approx 780 \text{ mAh g}^{-1}$ during the subsequent 160 cycles. The extraordinary long-term and high-rate performance suggests a superior cyclic reversibility and structural stability in the electrolyte.

Figure 4d compares the electrochemical performance between LHCA//GNS nanosheets (S1), high-quality graphite,^[38] and the most representative Co(II)-based materials, i.e., CoC_2O_4 nanoribbons,^[39] $\text{Co(OH)}_2/\text{GNS}$,^[40] CoO quantum dot/GNS,^[41] CoCO_3/GNS ,^[42] $\text{Co}_2(\text{OH})_3\text{Cl}/\text{GNS}$,^[43] and $\text{CoCl}_2 \cdot 6\text{H}_2\text{O}$ ^[43] (see details in Table S1, Supporting Information). The reversible capacity of graphite is 315 mAh g^{-1} after 50 cycles at the current density of only 37.2 mA g^{-1} . By sharp contrast, the reversible capacities of LHCA//GNS nanosheets are $\approx 1050 \text{ mAh g}^{-1}$ (after 200 cycles) and $\approx 780 \text{ mAh g}^{-1}$ (after 300 cycles) at 1000 and 4000 mA g^{-1} , respectively. In comparison with Co(II)-based materials, except $\text{Co}_2(\text{OH})_3\text{Cl}/\text{GNS}$, the LHCA//GNS composite exhibits much better long-term and/or high-rate performances, suggesting more competitive lithium storage potentials. Moreover, it exhibits high reversible capacities and good stability when assembled into full cells with commercial LiFePO_4 cathodes (Figure S5, Supporting Information).

2.4. Lithium Storage Mechanism of LHCA

Based on the conversion mechanism (Type III), the electron transfer should occur in the Co element of $\text{Co(Ac)}_{0.48}(\text{OH})_{1.52} \cdot 0.55\text{H}_2\text{O}$, i.e., Co^{2+} ions first reduce to Co^0 during discharging and recover to the original state when charging, giving a theoretical capacity of 462 mAh g^{-1} (equals to 2 Li storage). Obviously, the presented reversible capacities of pure LHCA and composites (S1–S3) are much higher. Taking S1 as a typical example (Figure 5a), the reversible Li ion numbers at 350 mA g^{-1} are 4.58 (2.29 times the theoretical value) for the initial 2 cycles, 4.22 (2.11 times) for the 10th cycle, 3.78 (1.89 times) for the 20th cycle, 3.15 (1.58 times) for the 40–80 cycles, and 3.80 (1.90 times) for the 100–120 cycles. From where does the huge extra capacity originate?

LHCA herein should work on a novel model—the electrocatalytic conversion mechanism (Type IV)—where the other elements besides Co should also participate in electron transfer and contribute considerable capacity. Similar instances occur in the lithium storage process of transition metal carbonates^[12] and $\text{RuO}_2 \cdot \gamma\text{H}_2\text{O}$.^[15] For example, with the help of GNS,

CoCO_3 exhibited 2.2 times higher reversible capacity than the theoretical value of 450 mAh g^{-1} according to the conversion mechanism.^[12,44,45] Ex-situ XRD, HRTEM, and XPS showed that C^{4+} in CO_3^{2-} also participated in the Li^+ /electron transfer and converted to low-valence carbon (such as Li_xC_2 , where $x = 0, 1, 2$). The highly active Co nanoparticles can chemically combine with $\text{C}=\text{O}$ bonds, reduce reaction activation energy, and hence promote the electrocatalytic efficiency. In contrast to CoCO_3 , FT-IR and XPS confirmed that the number of conjunction double bonds ($\text{C}=\text{O}$ and $\text{C}=\text{C}$) in LHCA is very small (as shown in Figure 1), and cannot afford enough sites for lithium storage. The cyclic voltammetric (CV) curves in Figure 5b also show that the redox reactions in LHCA and CoCO_3 are obviously different. Instead, LHCA possesses a large amount of Ac^- and OH^- ions, which are converted into LiAc and LiOH in the discharge process, respectively. More recently, Grey and co-workers confirmed the reversible reaction of LiOH to Li_2O and LiH under the existence of Ru nanocatalysts through high-resolution solid-state NMR techniques together with theoretical computations.^[15]

FT-IR spectra of pure LHCA electrodes were recorded to further detect the change of Ac^- ions during cycling (Figure 6). Clearly in Figure 6a, the electrode after charging exhibits very similar profile to that before cycling, indicating good reversibility. However, there is a significant difference between the electrodes before cycling and after the initial discharge. Figure 6b compares FT-IR curves of LHCA electrodes after discharging with acetic acid and acetaldehyde. Totally speaking, LHCA electrodes after discharging combine the character of both acetic acid and acetaldehyde, implying the presence of acetates after lithiation and its partial conversion to acetaldehyde. The strong peaks at 1720 and 1340 cm^{-1} are the characteristic $\nu_s(\text{C}=\text{O})$ and $\delta(-\text{CH})$ vibration of acetaldehyde, respectively. The conversion between acetates and acetaldehyde has been widely reported with the electrocatalyst of transition metals and oxides.^[16–22]

Based on the above considerations, we anticipate that the main reactions can be presented as

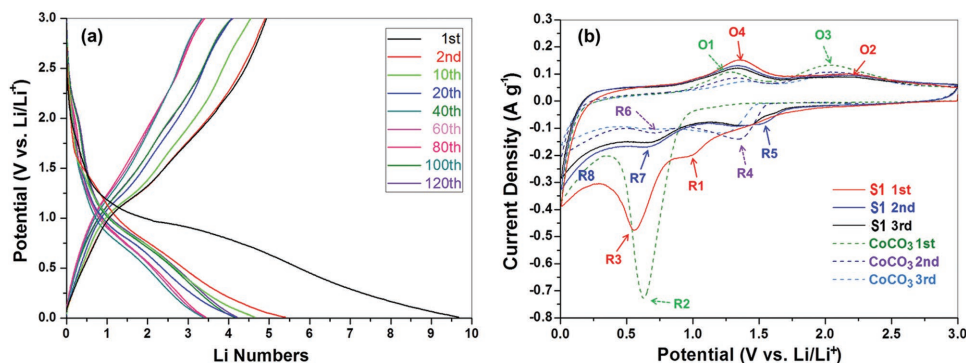
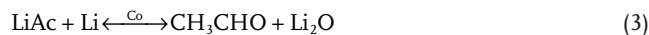
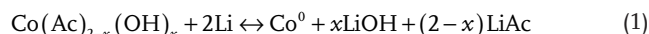


Figure 5. a) Charge–discharge profiles of S1 for different cycles at the current density of 350 mA g^{-1} . b) CV curves of pure CoCO_3 and S1.

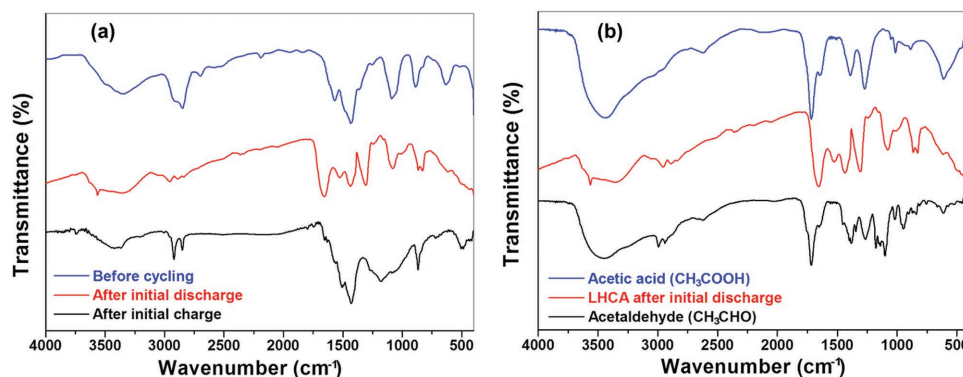


Figure 6. FT-IR spectra. a) Pure LHCA electrodes before cycling, after the initial discharge and after the initial charge. b) Pure LHCA electrodes after the initial discharge, acetic acid (CH_3COOH), and acetaldehyde (CH_3CHO).

According to this proposal, $\text{Co}(\text{Ac})_{0.48}(\text{OH})_{1.52} \cdot 0.55\text{H}_2\text{O}$ can store over five Li's, ≈ 2.5 times that on the basis of the traditional conversion mechanism, and can explain the huge extra capacity phenomenon very well. The proposed reactions match the charge/discharge profiles and CV curves very well (Figure 5). Taking CV as an example, the first reduction peak (R5) at around 1.5 V belongs to Equation (1), i.e., the lithiation and decomposition of LHCA to Co^0 , LiOH, and LiAc. The second reduction peak (R7) at ≈ 0.7 V corresponds to Equations (2) and (3) where, under the electrocatalysis of newly generated Co^0 nanoparticles, LiOH and LiAc further react with Li into $\text{Li}_2\text{O}/\text{LiH}$ and acetaldehyde, respectively.^[15] Correspondingly, there are two oxidation peaks in the charge process: O2 at ≈ 2.1 and O4 at ≈ 1.5 V. The potential difference of reduction and oxidation peaks widely exists in the electrodes and generally originates from the polarization along with the lithiation and delithiation processes.^[46,47] The low-voltage peak (R8) at 0.3–0 V can be mainly ascribed to GNS. Note that the high capacity retention (Figure 4), similar charge/discharge profiles, and almost overlapped CV curves (Figure 5) elucidate good reversibility of the proposed reactions to a great extent.

Note that the SEI films herein should also provide partial capacity during cycling, similar to the extra capacity (generally $100\text{--}200 \text{ mAh g}^{-1}$) in metal oxide anodes. However, it is far from the $\approx 150\%$ higher reversible capacity of LHCA than the theoretical value (462 mAh g^{-1}) on the basis of the conversion mechanism. Most of the extra capacity should originate from the conversion of LiOH and LiAc, both of which are very limited in the SEI films and can be neglected in comparison with that in the LHCA electrodes.^[48] In another word, the SEI components LiOH and LiAc can exactly store lithium with the electrocatalysis of Co metal nanoparticles, whereas LHCA herein enhances this phenomenon hugely.

3. Conclusions

In summary, LHCA was introduced as a promising anode material in LIBs for the first time. Furthermore, LHCA was successfully prepared into ultrathin nanoplates and face-to-face anchored on the surface of few-layered GNS through a facile one-pot solvothermal method. The parallel contact between

LHCA nanoplates and GNS was preferable for improving the electronic transport and avoiding the agglomeration during repeated charge/discharge cycles. As a result, LHCA//GNS nanosheets exhibited ultrahigh long-term reversible capacity and extraordinary high-rate performance. FT-IR confirms the conversion from acetate to acetaldehyde. A reasonable mechanism is proposed to elucidate the lithium storage behaviors referring to the electrocatalytic conversion of the OH group with Co^0 metal nanocatalysts. This work can help us further understand the contribution of SEI components (especially LiOH and LiAc) for lithium storage and disclose new paths to develop advanced materials for next-generation energy storage devices. Therefore, layered transition metal hydroxides ($\text{M}(\text{A})_x(\text{OH})_{2-x} \cdot n\text{H}_2\text{O}$ where M is transition metal and A is Ac^- , NO_3^- , Cl^- , etc.) can be used as high-efficiency materials for lithium-ion batteries, sodium ion batteries, and supercapacitors.

4. Experimental Section

Preparation of Few-Layered GNS and LHCA/GNS Composites: All the concerned reagents were of analytic grade and used without further purification. GNS samples were prepared according to the previous report.^[12] Three LHCA/GNS samples (denoted as **S1**, **S2**, and **S3**) were synthesized by using different amounts of cobaltous acetate (CA , $\text{Co}(\text{CH}_3\text{COO})_2 \cdot 4\text{H}_2\text{O}$) of 0.063, 0.147, and 0.566 g, respectively. Taking **S1** as an example, 0.03 g GNS, 0.063 g CA, and 0.75 g urea were homogeneously dispersed in 30 mL EG under vigorous stirring and ultrasonic treatment for 60 min separately. The obtained suspension was placed to a 50 mL Teflon-sealed autoclave and maintained at 200°C in an oven for 2 h. The products were centrifuged and washed with ethanol at least five times, and dried at 60°C overnight for further characterization. As a reference, pure LHCA was prepared at the same conditions but without GNS addition.

Material Characterization: XRD was conducted under Rigaku D/Max III diffractometer with Cu $K\alpha$ radiation ($\lambda = 1.5418 \text{ \AA}$). AFM was tested at MMAFM/STM, D3100M, Digital Ltd. SEM was tested using a Hitachi S-4700 (operated at 15 kV) and FEI Nanosem 430 field-emission gun scanning electron microscope. TEM, HRTEM, SAED, and energy dispersive X-ray spectroscopy were measured using a Tecnai G²F30 S-Twin (operated at 300 kV) and FEI Tecnai G²F-20 field-emission gun transmission electron microscope. TGA was obtained using Rigaku PTC-10A TG-DTA analyzer in air at $10^\circ\text{C min}^{-1}$. FT-IR (Bio-rad FTS6000), elementary analyzer (vario EL CUBE, elementar), and XPS (Axis Ultra DLD, Kratos Analytical Ltd.) were performed to confirm the chemical composition of LHCA.

Electrochemical Measurements: The active materials were made into working electrodes and tested in 2032-type cells. The working electrodes were comprised of active materials, acetylene black and polytetrafluoroethylene at the weight ratio of 80:10:10. The average weight of the working electrodes was $\approx 1.5 \text{ mg cm}^{-2}$. Lithium metal was used as the counter and reference electrode. The electrolyte was 1 M LiPF_6 dissolved in a 1:1:1 mixture of ethylene carbonate, ethylene methyl carbonate, and dimethyl carbonate. The cells were assembled in a glove box filled with high-purity argon (O_2 and $\text{H}_2\text{O} < 1 \text{ ppm}$). Cycling measurements were performed between the potential range of 0.01 and 3.00 V (vs Li/Li⁺) under a LAND-CT2001A instrument at room temperature. All the tested capacities are based on the whole weight of samples. CV was performed at a scanning rate of 0.1 mV s^{-1} between 0.01 and 3.00 V (vs Li/Li⁺). EIS was taken under a Solartron SI1287 + SI1260 potentiometer at 25 °C with the frequency range from 10 kHz to 10 mHz and an AC signal of 5 mV in amplitude as the perturbation.

Supporting Information

Supporting Information is available from the Wiley Online Library or from the author.

Acknowledgements

L.S. and J.H. contributed equally to this work. This work was supported by the National Natural Science Foundation of China (21403195 and 21421001) and the Key Research and Development Program (2015C01001) of Science and Technology Department of Zhejiang Province. Prof. Xue Qin of Tianjin University is gratefully acknowledged for his help with the preparation and characterization of graphene nanosheets.

Received: October 23, 2016

Revised: December 12, 2016

Published online: January 19, 2017

- [1] Y. Zhang, Y. Zhao, J. Ren, W. Weng, H. Peng, *Adv. Mater.* **2015**, *28*, 4524.
- [2] Y. Zhong, M. Yang, X. Zhou, Z. Zhou, *Mater. Horiz.* **2015**, *2*, 553.
- [3] E. Uchaker, G. Z. Cao, *Nano Today* **2014**, *9*, 499.
- [4] L. Ji, Z. Lin, M. Alcoutlabi, X. Zhang, *Energy Environ. Sci.* **2011**, *4*, 2682.
- [5] M. Winter, J. O. Besenhard, M. E. Spahr, P. Novák, *Adv. Mater.* **1998**, *10*, 725.
- [6] V. Etacheri, R. Marom, R. Elazari, G. Salitra, D. Aurbach, *Energy Environ. Sci.* **2011**, *4*, 3243.
- [7] J. R. Szczech, S. Jin, *Energy Environ. Sci.* **2011**, *4*, 56.
- [8] C.-M. Park, J.-H. Kim, H. Kim, H.-J. Sohn, *Chem. Soc. Rev.* **2010**, *39*, 3115.
- [9] P. Poizot, S. Laruelle, S. Grugeon, L. Dupont, J. M. Tarascon, *Nature* **2000**, *407*, 496.
- [10] L. Ma, J. Ye, W. Chen, D. Chen, J. Y. Lee, *Nano Energy* **2014**, *10*, 144.
- [11] M. V. Reddy, G. V. Subba Rao, B. V. Chowdari, *Chem. Rev.* **2013**, *113*, 5364.
- [12] L. Su, Z. Zhou, X. Qin, Q. Tang, D. Wu, P. Shen, *Nano Energy* **2013**, *2*, 276.
- [13] Y. Zhong, M. Yang, X. Zhou, Y. Luo, J. Wei, Z. Zhou, *Adv. Mater.* **2015**, *27*, 806.
- [14] L. Su, Y. Zhong, Z. Zhou, *J. Mater. Chem. A* **2013**, *1*, 15158.
- [15] Y. Y. Hu, Z. Liu, K. W. Nam, O. J. Borkiewicz, J. Cheng, X. Hua, M. T. Dunstan, X. Yu, K. M. Wiaderek, L. S. Du, K. W. Chapman, P. J. Chupas, X. Q. Yang, C. P. Grey, *Nat. Mater.* **2013**, *12*, 1130.
- [16] R. Pestman, R. M. Koster, E. Boellaard, A. M. van der Kraan, V. Ponec, *J. Catal.* **1998**, *174*, 142.
- [17] W. Rachmady, M. A. Vannice, *J. Catal.* **2000**, *192*, 322.
- [18] G. C. Tustin, L. S. Depew, N. A. Collins, *US Patent 6121498*, **2000**.
- [19] X. Zhang, Y. Le, Z. Gao, *Chem. J. Chin. Univ.* **2003**, *24*, 121.
- [20] K. B. Kokoh, F. Hahn, E. M. Belgsir, C. Lamy, A. R. de Andrade, P. Olivi, A. J. Motheo, G. Tremiliosi-Filho, *Electrochim. Acta* **2004**, *49*, 2077.
- [21] M. Heinen, Z. Jusys, R. J. Behm, *J. Phys. Chem. C* **2010**, *114*, 9850.
- [22] V. J. Johnston, J. H. Zink, L. Chen, B. F. Kimmich, J. T. Chapman, W. J. C. Van Der, V. Zuzaniuk, *US Patent 7816565*, **2010**.
- [23] L. Poul, N. Jouini, F. Fiévet, *Chem. Mater.* **2000**, *12*, 3123.
- [24] D. Zheng, Y. Wang, L. Shi, S. Sun, *Chem. Res. Chin. Univ.* **2011**, *27*, 910.
- [25] K. Suzuki, J. Haines, P. Rabu, K. Inoue, M. Drillon, *J. Phys. Chem. C* **2008**, *112*, 19147.
- [26] S. Švarcová, M. Klementová, P. Bezdička, W. Łasocho, M. Dušek, D. Hradil, *Cryst. Res. Technol.* **2011**, *46*, 1051.
- [27] N. Masciocchi, E. Corradi, A. Sironi, G. Moretti, G. Minelli, P. Porta, *J. Solid State Chem.* **1997**, *131*, 252.
- [28] G. X. Wu, H. S. Wu, X. M. Zhang, *Dalton Trans.* **2010**, *39*, 1179.
- [29] Y. Park, D. S. Shin, S. H. Woo, N. S. Choi, K. H. Shin, S. M. Oh, K. T. Lee, S. Y. Hong, *Adv. Mater.* **2012**, *24*, 3562.
- [30] F. Wan, X.-L. Wu, J.-Z. Guo, J.-Y. Li, J.-P. Zhang, L. Niu, R.-S. Wang, *Nano Energy* **2015**, *13*, 450.
- [31] C. Wang, Y. Xu, Y. Fang, M. Zhou, L. Liang, S. Singh, H. Zhao, A. Schober, Y. Lei, *J. Am. Chem. Soc.* **2015**, *137*, 3124.
- [32] L. Su, X. Wu, J. Hei, L. Wang, Y. Wang, *Part. Part. Syst. Charact.* **2015**, *32*, 721.
- [33] D. Chen, H. Feng, J. Li, *Chem. Rev.* **2012**, *112*, 6027.
- [34] Y. Sun, Q. Wu, G. Shi, *Energy Environ. Sci.* **2011**, *4*, 1113.
- [35] F.-Y. Su, Y.-B. He, B. Li, X.-C. Chen, C.-H. You, W. Wei, W. Lv, Q.-H. Yang, F. Kang, *Nano Energy* **2012**, *1*, 429.
- [36] L. Su, J. Jiang, L. Wang, Y. Wang, M. Ren, *ChemElectroChem* **2015**, *2*, 789.
- [37] G. Zhou, D.-W. Wang, F. Li, L. Zhang, N. Li, Z.-S. Wu, L. Wen, G. Q. Lu, H.-M. Cheng, *Chem. Mater.* **2010**, *22*, 5306.
- [38] N. Cuesta, A. Ramos, I. Cameán, C. Antuña, A. B. García, *Electrochim Acta* **2015**, *155*, 140.
- [39] M. J. Aragon, B. Leon, C. P. Vicente, J. L. Tirado, A. V. Chadwick, A. Berko, S. Y. Beh, *Chem. Mater.* **2009**, *21*, 1834.
- [40] X. L. Huang, J. Chai, T. Jiang, Y. J. Wei, G. Chen, W. Q. Liu, D. X. Han, L. Niu, L. M. Wang, X. B. Zhang, *J. Mater. Chem.* **2012**, *22*, 3404.
- [41] C. Peng, B. Chen, Y. Qin, S. Yang, C. Li, Y. Zuo, S. Liu, J. Yang, *ACS Nano* **2012**, *6*, 1074.
- [42] M. A. Garakani, S. Abouali, B. Zhang, C. A. Takagi, Z. L. Xu, J. Q. Huang, J. Huang, J. K. Kim, *ACS Appl. Mater. Interfaces* **2014**, *6*, 18971.
- [43] G. D. Park, J.-H. Lee, Y. C. Kang, *Carbon* **2015**, *84*, 14.
- [44] Z. Ding, B. Yao, J. Feng, J. Zhang, *J. Mater. Chem. A* **2013**, *1*, 11200.
- [45] N. Tian, C. Hua, Z. Wang, L. Chen, *J. Mater. Chem. A* **2015**, *3*, 14173.
- [46] H. X. Yang, Q. F. Dong, X. H. Hu, X. P. Ai, S. X. Li, *J. Power Sources* **1999**, *79*, 256.
- [47] S. Laruelle, S. Grugeon, P. Poizot, M. Dollé, L. Dupont, J. M. Tarascon, *J. Electrochem. Soc.* **2002**, *149*, A627.
- [48] S.-C. Kinoshita, M. Kotato, Y. Sakata, M. Ue, Y. Watanabe, H. Morimoto, S.-I. Tobishima, *J. Power Sources* **2008**, *183*, 755.